Evaluation of *trans*- and *cis*-4-[^{18}F]fluorogabapentin for brain PET imaging

Authors:

Yu-Peng Zhou[1,#], Marc D. Normandin[1,#], Vasily Belov[1], Marina T. Macdonald-Soccorso[1], Sung-Hyun Moon[1], Yang Sun[1], Georges El Fakhri[1], Nicolas J. Guehl[1,*] and Pedro Brugarolas[1,*]

[#] Equal contribution

* Co-corresponding authors

Affiliations:

[1] Gordon Center for Medical Imaging, Department of Radiology, Massachusetts General Hospital and Harvard Medical School, Boston, Massachusetts.

Correspondence

Pedro Brugarolas, PhD
55 Fruit St
Bulfinch 051
Boston, MA 02114
pbrugarolas@mgh.harvard.edu

Nicolas J. Guehl, PhD
55 Fruit St
White 427
Boston, MA 02114
nguehl@mgh.harvard.edu

ABSTRACT

Gabapentin, a selective ligand for the α2δ subunit of voltage-dependent calcium channels, is an anticonvulsant medication used in the treatment of neuropathic pain, focal epilepsy and other neurological conditions. We recently described two radiofluorinated derivatives of gabapentin (*trans*-4-[^{18}F]fluorogabapentin, [^{18}F]tGBP4F, and *cis*-4-[^{18}F]fluorogabapentin, [^{18}F]cGBP4F) and showed that these compounds preferentially accumulate in the injured nerves and spinal cord in a rodent model of neuropathic pain. Given the use of gabapentin in brain diseases, we set out to test whether these radiofluorinated derivatives of gabapentin could be used for imaging α2δ receptors in the brain. Specifically, we developed fully automated radiosynthesis methods for [^{18}F]tGBP4F and [^{18}F]cGBP4F and conducted dynamic PET imaging of the brain in two adult rhesus macaques with and without pre-administration of pharmacological doses of gabapentin. These radiotracers showed high metabolic stability, negligible plasma protein binding, moderate-to-low brain penetration and very slow kinetics. Kinetic modeling of brain regional time-activity curves using a metabolite-corrected arterial input function shows that 1-tissue compartment model accurately fits the data. Graphical analysis via Logan and multilinear analysis 1 produced similar results as compartmental modeling indicating robust quantification. Despite these favorable properties, the limited brain penetration and inability to displace the signal via pharmacological challenge suggests that tracers with higher brain penetration may be needed to image α2δ expression in the brain.

KEYWORDS

Radiotracer, PET, fluorine-18, gabapentin, brain imaging, voltage gated calcium channels, α2δ-1

INTRODUCTION

Gabapentin targets the α2δ subunit of voltage-gated calcium channels (VGCC) expressed throughout the central and peripheral nervous systems (CNS and PNS)[1,2]. Four subunits of α2δ (α2δ-1 through 4) have been identified and their expression is altered in multiple diseases. For instance, the expression of α2δ-1 in the PNS or CNS is greatly increased in models of neuropathic pain[3-9], neuroinflammation[10,11] and addiction[12-17] whereas α2δ-1 protein is downregulated in an animal model of epilepsy[18]. In addition, mutations in α2δ-2 are associated with seizures in animals and humans. As such, pharmacological modulation of α2δ with gabapentin results in clinical improvement of conditions such as partial seizures and neuropathic pain.

Given the role of α2δ in multiple CNS and PNS diseases, we hypothesized that imaging α2δ with a radiolabeled version of gabapentin would be valuable for understanding these diseases and could potentially serve as a diagnostic tool. In our prior work, we developed two radiofluorinated derivatives of gabapentin (*cis*- and *trans*-[^{18}F]4-fluorogabapentin or [^{18}F]cGBP4F and [^{18}F]tGBP4F) and found that these compounds bind to α2δ-1 with different affinities (24 nM for [^{18}F]cGBP4F and 2400 nM for [^{18}F]tGBP4F). We also found that these compounds accumulate 1.6- to 2-fold higher in the injured nerves than uninjured nerves of a rat model of neuropathic pain, which is consistent with the higher protein expression in these tissues.

Given the important role of α2δ subunits in CNS diseases, we decided to examine the [^{18}F]tGBP4F and [^{18}F]cGBP4F for brain imaging. Although these tracers have a low predicted partition coefficient (cLogP = -1.267), which suggests poor brain penetration, it is known that gabapentin enters the brain via the LAT1 transporter[19] and, thus, these tracers may have suitable brain penetration. To investigate the potential value of these tracers for brain PET imaging, we used non-human primates (NHPs) as their large brain size and similarities with the human brain make them excellent models to study brain tracers. Furthermore, to produce enough tracer for large animal studies, fully automated radiosynthesis methods were developed consistent with current good manufacturing practices (cGMP) and radiation safety regulations.

RESULTS

Automation of radiosynthesis

The radiosynthesis of PET tracers [^{18}F]tGBP4F and [^{18}F]cGBP4F has been previously reported[20]. Here, automated radiosynthesis methods were developed using a GE TRACERlab FX2N two-reactor synthesis module. Before starting the radiosynthesis, the reagents were loaded into the different vials as shown in **Figure 1**. In the first step, [^{18}F]fluoride was trapped in a QMA cartridge, eluted with H_2O/MeCN/kryptofix into reactor 1 and dried under reduced pressure and heating. The precursor **6a** or **6b** was then added to reactor 1 and radiofluorination was carried out at 140 ºC for 20 min forming intermediate **7a** or **7b**,

respectively (**Fig. 1**). Intermediate **7a** or **7b** was diluted in water and trapped on an HLB cartridge. Next, the intermediate **7a** or **7b** was eluted from the cartridge using acetonitrile and transferred into reactor 2 for hydrolysis and deprotection. Since the final product is hydrophilic, [^{18}F]tGBP4F or [^{18}F]cGBP4F was isolated by semi-preparative HPLC purification by using a mobile phase compatible for injection containing 5% EtOH in phosphate buffer. A typical run starts from 37 GBq (1.0 Ci) of [^{18}F]fluoride and yields 1.6 GBq (43 mCi) of [^{18}F]tGBP4F (non-decay corrected radiochemical yield: 4.3 ± 2.2 % (n = 13)) or 0.52 GBq (14 mCi) [^{18}F]cGBP4F (non-decay corrected radiochemical yield: 1.4 ± 1.2 % (n = 3)) in ~120 min. The identity and purity (>99% of radiochemical purity) of [^{18}F]tGBP4F or [^{18}F]cGBP4F was confirmed by analytical radioHPLC (**Fig. S1**). The molar activities for[^{18}F]tGBP4F and [^{18}F]cGBP4F were greater than 1 Ci/µmol.

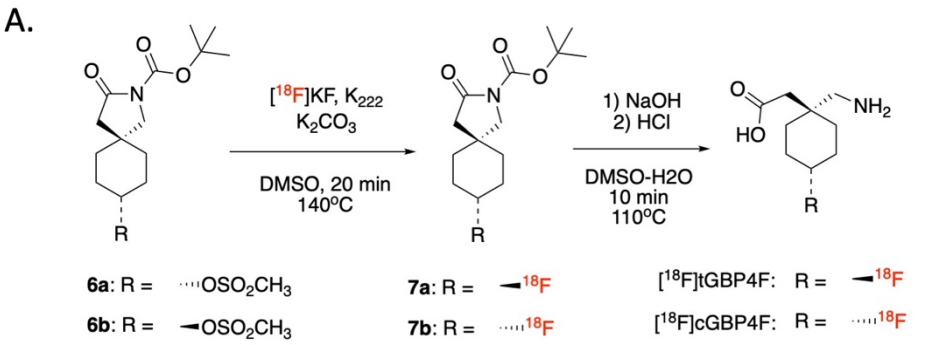

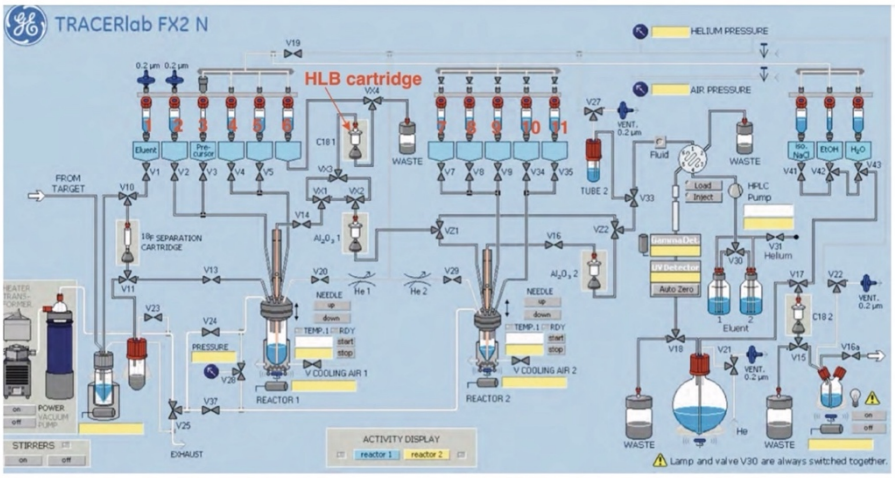

Vials	Reagent	Vials	Reagent
1	1mL of acetonitrile/water (1:1) solution of Kryptofix 2.2.2 (K_{222}, 15 mg) and K_2CO_3 (1.25 mg)	7	0.3 mL of NaOH solution (5N)
2	6 mL of sterile water	8	0.6 mL of HCl solution (6N)
3	0.3 mL of anhydrous DMSO solution of precursor	9	0.2 mL of NaOH solution (5N)
4	1 mL of anhydrous acetonitrile	10	2 mL of sterile water
5	6 mL of sterile water	11	1.5 mL of $NaHCO_3$ solution (1M)
6	2 mL of acetonitrile		

Figure 1. Automated production of [^{18}F]tGBP4F and [^{18}F]cGBP4F. **A.** Radiochemical synthesis of [^{18}F]tGBP4F and [^{18}F]cGBP4F**. B**. Flow diagram of the synthesis module used in the synthesis (GE TRACERlab FX2 N) and table of reagents.

Blood analysis

Two rhesus macaques underwent paired baseline and blocking PET scans with either [^{18}F]tGBP4F or [^{18}F]cGBP4F within 3 months of each other. For blocking scans, animals were injected with gabapentin (4.7 mg/kg for the [^{18}F]tGBP4F scan; 5.0 mg/kg for the [^{18}F]cGBP4F scan) 30 min before radiotracer injection.

Serial arterial blood samples were collected at various time points during each PET scan and were analyzed for radioactivity concentrations in whole blood (WB) and plasma (PL). Selected plasma samples were analyzed by radio-HPLC to measure the parent fraction in plasma (PP). The plasma free fraction (f_p) was also measured. The WB and parent in PL curves peaked at ~3.5 min after radiotracer injection and the clearance following the peak was best described by a biexponential curve (**Fig 2** and **Fig. S2**). The half-lives of the rapid and slow components are shown in **Table 1** for each tracer ([^{18}F]cGBP4F and [^{18}F]tGBP4F) and condition (baseline and blocking). The clearance was moderately fast (10.9 min for the *cis*- and 21.8 min for the *trans*-) for both compounds and it became slightly slower under blocking conditions (15.3 min and 24.9 min, respectively).

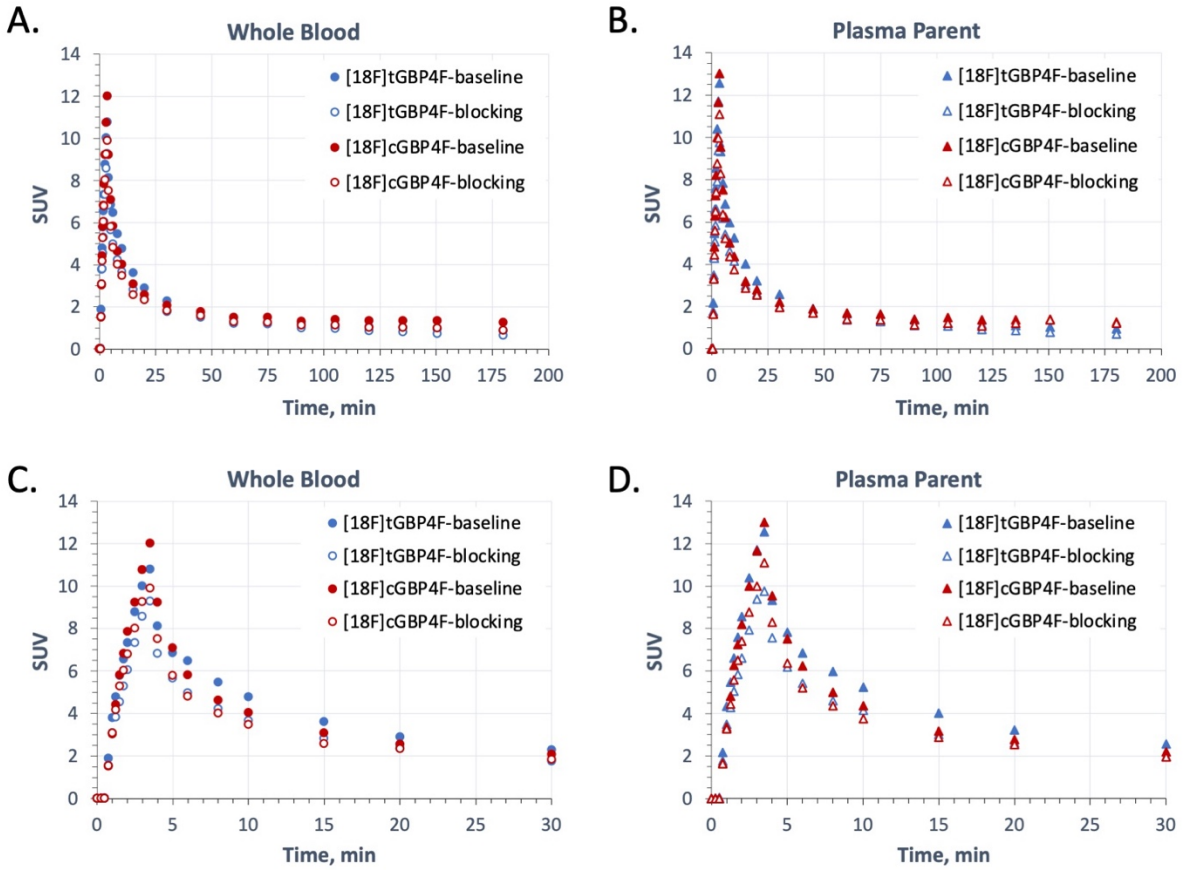

Figure 2. Blood and plasma concentrations of [^{18}F]tGBP4F and [^{18}F]cGBP4F. **A.** Time courses of radioactivity concentrations in arterial whole blood under baseline and blocking conditions. **B.** Time courses of radioactivity concentrations in plasma under baseline and blocking conditions. **C.** and **D**. Magnification of the first 30 min of **A** and **B**, respectively.

The plasma free fraction (f_p) averaged 1.01 ± 0.03 across studies for each radiotracer, indicating negligible plasma protein binding. The WB to PL ratios reached equilibrium within 1 min and remained stable at near 0.9 for all scans (**Fig. S3**). RadioHPLC analysis of plasma samples suggested that both radiotracers undergo minimal *in vivo* metabolism (%PP range from 95% to 98% at 180 min post injection (**Fig. S4**).

Table 1. Whole blood clearance parameters from biexponential model fits (R^2 > 0.99 for all)

Tracer / condition	Fast clearance half-life (min)	Slow clearance half-life (min)	Plateau (SUV)
cGBP4F / baseline	1.16	10.9	1.63
cGBP4F / blocking	1.40	15.3	1.24
tGBP4F / baseline	3.2	21.8	1.092
tGBP4F / blocking	2.4	24.9	0.886

Brain PET imaging

Summed PET images of the monkey brains from 45-90 min show low brain penetration for [^{18}F]tGBP4F and moderate brain penetration for [^{18}F]cGBP4F (**Fig. 3A**). The time-activity curves (TACs) for [^{18}F]cGBP4F baseline scan peaked around 3.8 min (whole brain SUV = 0.55), followed by a sharp decrease (SUV = 0.45 at 9 min) and a slow accumulation in the brain (SUV at 180 min = 0.7) (**Fig. 3C**). Similarly, [^{18}F]tGBP4F TACs showed an initial peak (SUV = 0.4 at 3.8 min), followed by a decrease (SUV = 0.25 at 13 min) and a very slow accumulation in the brain (SUV = 0.28 at 180 min) (**Fig. 3D**). Within the brain, the areas with highest uptake were the amygdala, insula and nucleus accumbens for both tracers and the areas with lowest uptake were the thalamus, cerebellum and white matter.

In the case of [^{18}F]cGBP4F, pre-injection of 5 mg/kg of non-radioactive gabapentin resulted in a visible reduction in brain SUV form 45-90 min which is also evidenced by a reduction in the TACs across all brain regions (**Fig. 3A**). For [^{18}F]tGBP4F, pre-injection of 4.7 mg/kg of non-radioactive gabapentin did not result in an obvious change in tracer uptake or in the regional TACs (**Fig. 3B**). In order to better quantify the blocking effects compartmental modeling was performed.

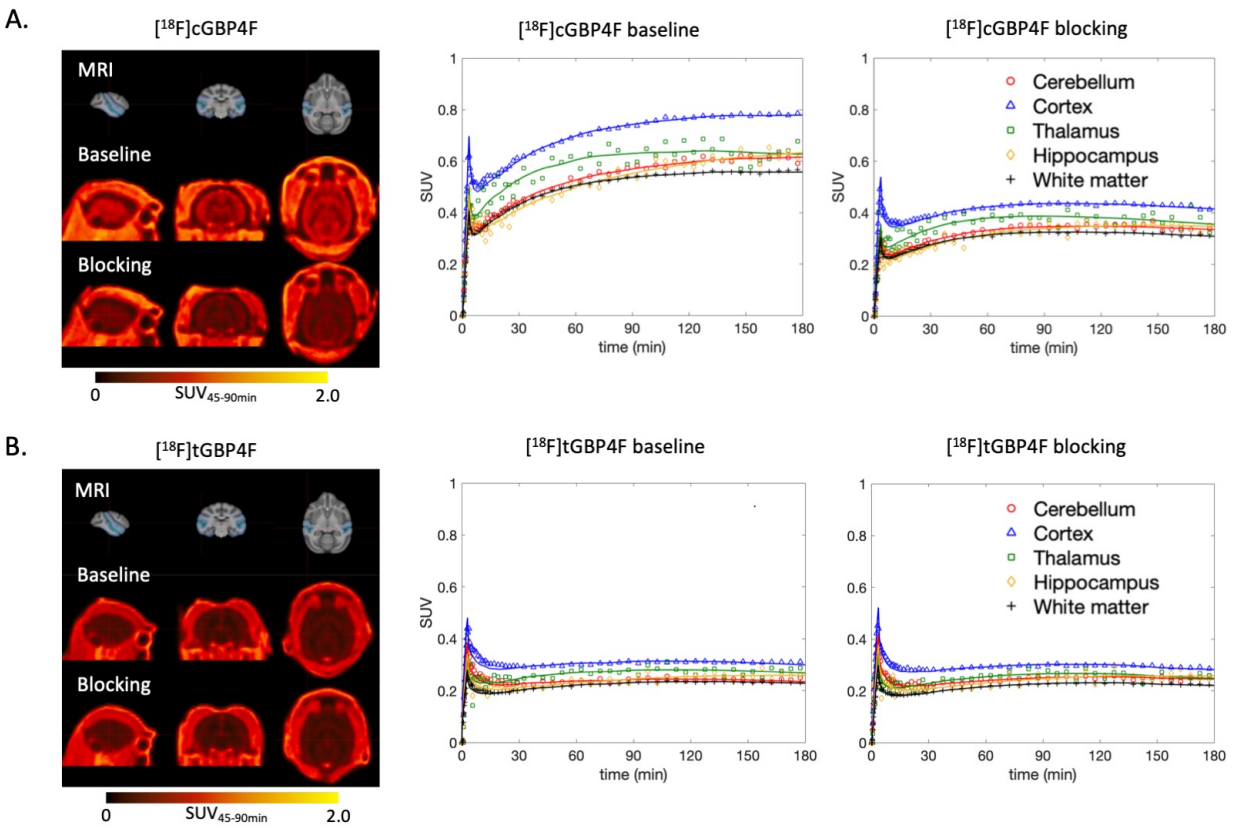

Figure 3. PET images and time activity curves of [^{18}F]cGBP4F and [^{18}F]tGBP4F under baseline and blocking conditions. **A.** PET SUV images showing the cerebral distribution of [^{18}F]cGBP4F under baseline and blocking conditions and corresponding regional time activity curves. **B.** PET SUV images showing the cerebral distribution of [^{18}F]tGBP4F under baseline and blocking conditions and corresponding regional time activity curves. Solid lines represent fitting from a 1TCM.

Modeling of the imaging data.

Kinetic modeling of the regional TACs was performed using 1-tissue and 2-tissue compartment models (1TCM and 2TCM) with fixed and variable vascular contribution using the whole scan duration (180 min) and after truncating the data to 120 and 90 min. A 1TCM with vascular contribution as a model parameter accurately fit the full TACs for both tracers and both conditions (**Fig. 3**).

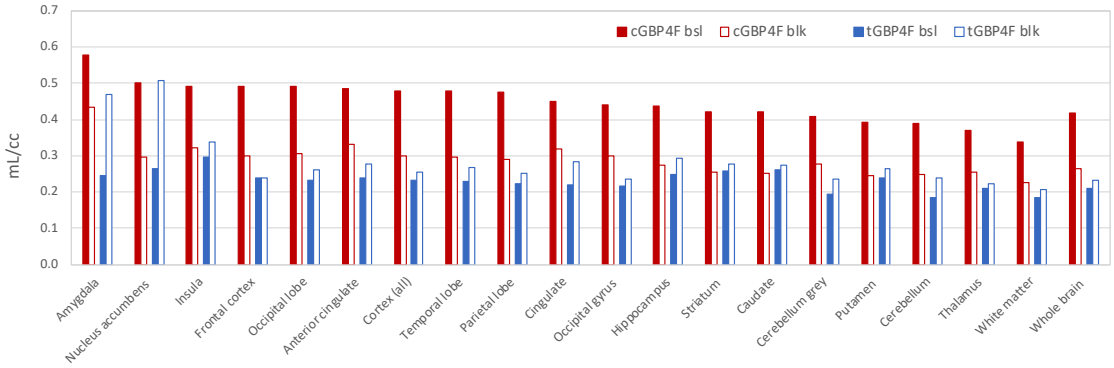

Figure 4. Regional V_T estimates obtained from the 1TCM for both tracers and conditions.

For [^{18}F]cGBP4F under baseline conditions, V_T values ranged from 0.58 mL/cc for the amygdala to 0.34 mL/cc for the white matter (**Fig. 4**) and K_1 values ranged from 0.0059 mL/min/cc for the occipital gyrus to 0.0029 mL/min/cc for the hippocampus. Under blocking conditions, the V_T and K_1 values for the whole brain decreased -36% and -35%, respectively. The correlation between changes in V_T and changes in K_1 across all brain regions (Pearson R = 0.479) suggests that the reduction in V_T may be driven by saturation of the LAT1 transporter but without retest data it is difficult to assess the significance.

In the case of [^{18}F]tGBP4F, V_T values ranged from 0.30 mL/cc for the insula to 0.18 mL/cc for the cerebellum (**Fig. 4**) and K_1 values ranged from 0.0021 mL/min/cc for the occipital gyrus to 0.0010 mL/min/cc for the amygdala. Under blocking conditions, the V_T and K_1 values for the whole brain increased by 11% and 16%, respectively. However, given the low V_T and K_1 values, and without retest data, it is not possible to determine if these changes are significant.

Graphical analysis using the Logan or multilinear analysis 1 (MA1) resulted in good linearization after 60 min (t* = 60 min) (**Fig. S5**). V_T values calculated with MA1 (**Fig. 5**) were in better agreement with V_T obtained from the compartmental analysis compared to those calculated with Logan (**Fig. S6**). Logan V_T suffered from a small underestimation and larger standard deviation (**Table 2**). Truncating the data to 120 or 90 min resulted in less robust V_T estimates and greater variability, as it would be expected given the slow kinetics.

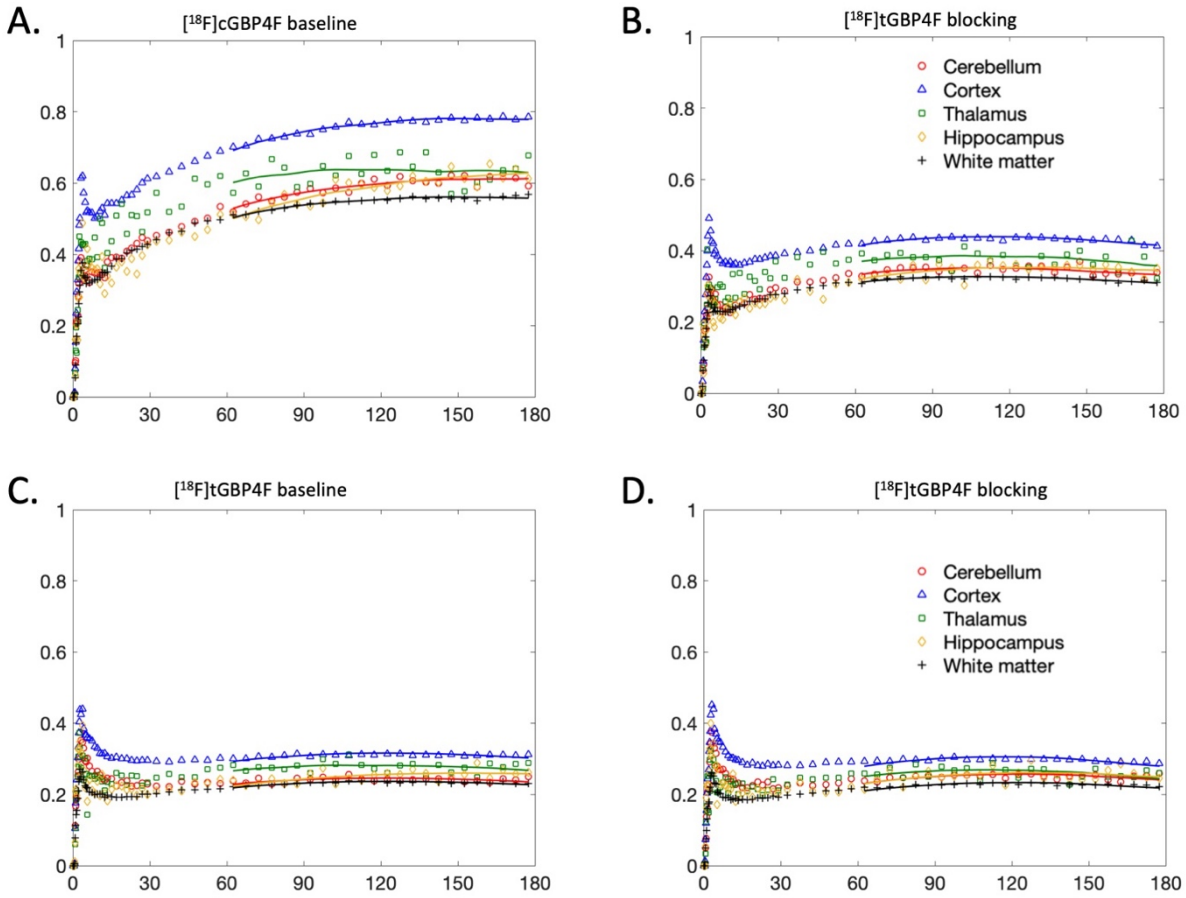

Figure 5. MA1 graphical analysis plots for [^{18}F]cGBP4F and [^{18}F]tGBP4F under baseline and blocking conditions. End time (t_{end}) of 180 min and a t* of 60 min were used for MA1 fits. MA1 fits to the data over the t* to t_{end} time interval is depicted for each representative ROI.

Table 2. Percent difference V_T *vs*. V_T 1T2kv

Tracer	Logan (180 min)	MA1 (180 min)
cGBP4F	-0.5 ± 7.9	3.2 ± 3.3
tGBP4F	-4.2 ± 13.1	0.8 ± 8.1

Discussion

The present study focuses on the evaluation of [^{18}F]tGBP4F and [^{18}F]cGBP4F, which have previously been found to have high and moderate affinity, respectively, to α2δ subunits in the brain of NHPs. Since α2δ subunits play a crucial role in various brain diseases, the development of tracers that can image these proteins in the brain is of great interest. In this study, an automated method was developed to produce sufficient quantities of tracers with high molar activity for NHP studies.

The NHP studies showed that the tracers are metabolically stable in blood and free of plasma protein binding. However, their brain penetration was found to be moderate to low, and their kinetics were very slow in the brain, not unlike what had previously been observed in rodents. The tracer kinetics across brain regions could accurately be described using a 1-tissue compartmental model which produced V_T values in the range 0.1 to 0.6 mL/cc for both tracers. When preinjected with gabapentin, [^{18}F]cGBP4F showed a -35% reduction in V_T and [^{18}F]cGBP4F showed a 16% increase. In the absence of test-retest data and given the moderate to low brain penetration it is difficult to assess the significance of these changes and whether the different effect upon drug challenge is due to blocking of the transporter, blocking of the receptor or experimental variability.

Despite having some favorable properties, the value of these tracers for imaging the brain may be limited. [^{18}F]cGBP4F has a modest binding affinity and moderate brain penetration and [^{18}F]tGBP4F has good binding affinity but low brain penetration.

In conclusion, while the investigation of [^{18}F]tGBP4F and [^{18}F]cGBP4F provides new information on the brain penetration and kinetics of GBP derivatives, the goal of imaging α2δ in the brain using PET remains elusive. Nevertheless, the findings of this study can be leveraged towards the development of novel tracers with better imaging properties and potentially as therapeutic agents for brain diseases involving α2δ subunits.

EXPERIMENTAL SECTION

Materials: Commercially available reagents were purchased from Sigma-Aldrich, Acros, Alfa-Assar or TCI and used as received.

Automated radiosynthesis of PET tracers: To start, target water from cyclotron was send to the QMA cartridge where [^{18}F]fluoride was trapped and eluted to reactor 1 by K_{222}/K_2CO_3 eluent. After drying the [^{18}F]fluoride, the precursor was added and then heated to 140°C for 20 min. sterile water (2 x 6mL) was added to the reactor 1 and the reaction mixture was sent to an HLB cartridge (see **Fig 1**). The labeled intermediate was trapped on the HLB cartridge and eluted into reactor 2 using 2 mL of acetonitrile. NaOH

and HCl solutions were added to reactor 2 and heated to 120°C for 5 min, respectively. Additional NaOH was added to neutralize the solution and vacuum was applied to remove acetonitrile. 2 mL of sterile water and 1.5 mL of $NaHCO_3$ solution (1M) were then added to the reactor 2 and the mixtures were transferred to TUBE 2 for HPLC purification. 4-[^{18}F]fluorogabapentin was isolated by semi-preparative HPLC using a XBridge 5μm C18 prep-column (10 x 250 mm) with a mobile phase of NaH_2PO_4 EtOH-H_2O (10mM, v/v = 5:95, pH = 8) at flow rate of 4 mL/min.

Animal experiments

Compliance: All experiments involving non-human primates were performed in accordance with the U.S. Department of Agriculture (USDA) Animal Welfare Act and Animal Welfare Regulations (Animal Care Blue Book), Code of Federal Regulations (CFR), Title 9, Chapter 1, Subchapter A, Part 2, Subpart C, §2.31. 2017. Animal experiments were approved by the Animal Care and Use Committee at the Massachusetts General Hospital (MGH).

Non-human primates (NHPs): Two male adult rhesus macaques (Monkey 1 and Monkey 2) were used in this study (ages: 13 and 17 years old, respectively). Animal body weights on the days of imaging were 13.26 kg (baseline scan) and 12.78 kg (blocking scan) for Monkey 1 and 15.96 kg (baseline scan) and 14.54 kg (blocking scan) for Monkey 2.

PET/CT imaging of NHPs: Two rhesus macaques (Monkey 1 and Monkey 2) were scanned on a Discovery MI (GE Healthcare) PET/CT scanner. Prior to PET/CT scan, monkeys were sedated with ketamine/xylazine (10/0.5 mg/kg IM) and were intubated for maintenance anesthesia with isoflurane (1-2% in 100% O_2). A venous catheter was placed in the saphenous vein for radiotracer injection and an arterial catheter was placed in the posterior tibial artery for blood sampling. The animal was positioned on a heating pad on the bed of the scanner for the duration of the study. A CT scan was acquired prior each PET acquisition for attenuation correction. PET data were acquired in 3D list mode for 180 min following injection of radiotracers. Radiotracers were administered *via* the lateral saphenous vein over a 3-minute infusion and followed by a 3-minute infusion of a saline flush. For the blocking scans, gabapentin (4.7 mg/kg for the [^{18}F]tGBP4F scan and 5.0 mg/kg for the [^{18}F]cGBP4F scan in 10 mL of saline) was administered 30 min prior to the administration of the radiotracer followed by 10 mL saline flush. All injections were performed using syringe pumps (Medfusion 3500). Dynamic PET data were reconstructed using a validated fully 3D time-of-flight iterative reconstruction algorithm using 3 iterations and 34 subsets while applying corrections for scatter, attenuation, deadtime, random coincident events, and scanner normalization. For all dynamic scans, list mode data were framed into dynamic series of 6x10, 8x15, 6x30, 8x60, 8x120s and

remaining were 300 s frames. Final reconstructed images had voxel dimensions of 256 x 256 x 89 and voxel sizes of 1.17 x 1.17 x 2.8 mm^3.

Magnetic resonance imaging: For each monkey, a three-dimensional structural T1-weighted magnetization-prepared rapid gradient-echo (MEMPRAGE) magnetic resonance (MR) image was acquired using a 3T Biograph mMR (Siemens Medical Systems) for anatomical reference. Acquisition parameters were as follows: repetition time = 2530 ms; echo time = 1.69 ms; inversion time = 1100 ms; flip angle = 7; voxel size = 1 X 1 X 1 mm^3; matrix size = 256 X 256 X 176; number of averages = 4.

Arterial blood sampling and analysis of radiometabolites: Arterial blood sampling was performed during the PET acquisitions. Samples of 1 to 3 mL were initially drawn every 30 seconds upon radiotracer injection and decreased in frequency to every 15 minutes toward the end of the scan. Radiotracer metabolism was characterized from blood samples acquired at 5, 10, 15, 30, 60, 90, 120 and 180 minutes. An additional blood sample of 3 mL was drawn prior tracer injection in order to measure the plasma free fraction (f_p). Radioactivity concentration (kBq/cc) was measured in whole-blood (WB) and subsequently in plasma (PL) following the centrifugation of WB. Radiometabolite analysis was performed using an automated column switching radioHPLC system[21,22]. Eluent was collected in 1-minute intervals and assayed for radioactivity using a Wallac Wizard gamma counter (1470 model). The procedure adopted for these measurements was similar to the one described previously[23,24], except for the mobile phases used. Injected plasma samples were initially trapped on the catch column using a mobile phase consisting of either 99:1 10 mM ammonium bicarbonate pH 8 in water:MeCN at 1.8 mL/min and the catch column was backflushed with 95:5 10 mM ammonium phosphate pH 8 in water:EtOH at 1 mL/min and the sample directed onto the analytical column. SUV-radioactivity time courses in WB and in PL were generated by correcting radioactivity concentrations (C [kBq/ml]) for injected dose (ID [MBq]) and animal body weight (BW [kg]) and were calculated as SUV(t) = C(t)/(ID/BW). Measured time courses of percent parent in plasma (%PP(t)) were fitted with a single exponential decay plus a constant. Individual metabolite-corrected arterial input functions ($C_p\ (t)$) were derived by correcting the total PL radioactivity concentration $C_p^{total}\ (t)$ for radiotracer metabolism using individual *%PP(t)*: $C_p\ (t) = C_p^{total}\ (t) \times \%PP(t)/100\%$[23,24]. The plasma free fractions were measured in triplicate by ultrafiltration following a procedure described previously[23,24]. Briefly, arterial plasma samples of 200 microliters, drawn before radiotracer injection, were spiked with ~444 kBq of [^{18}F]tGBP4F or [^{18}F]cGBP4F. Following a 15 min incubation period, radioactive plasma samples were loaded on ultrafiltration tubes (Millipore Centrifree) and centrifuged at 1,500 g for 15 min at room temperature. f_p was calculated as the ratio of free ultrafiltrate to plasma concentration and corrected for binding to the ultrafiltration tube membrane.

Image registration and processing: All PET processing was performed with an in-house developed Matlab software that uses FSL[25]. Individual brain MR and PET images were aligned into the MRI National Institute of Mental Health macaque template (NMT)[26] according to the following procedure. An early summed PET image (0-10 min post tracer injection) was rigidly co-registered to the animal's individual MEMPRAGE MR image which was subsequently registered into the NMT template space using a 12-parameter affine transformation followed by non-linear warping. The transformation matrices were then combined and applied inversely on the rhesus atlases in order to warp all atlases into the native PET image space for extraction of TACs. The composite regions of interest (ROIs) were derived from the two sets of digital anatomical atlases aligned to the NMT space. These were *Paxinos et al.* rhesus brain regions[27] previously aligned to the *McLaren et al.* rhesus MRI brain template[28] as well as the INIA19 NeuroMaps rhesus atlas[29]. Briefly, the T1 weighted average MR images of each template were transformed to the NMT template using a 12-parameter affine registration and non-linear warping both weighted on the brain (i.e. after skull stripping). The obtained transformation matrices were then applied to the composite ROIs. Regional TACs were extracted from the native PET image space for the following ROIs: amygdala, caudate, cerebellum grey, insula, nucleus accumbens, occipital gyrus, putamen , parietal lobe, temporal lobe, anterior cingulate, striatum, cerebellum no vermis (whole), cingulate, cortex (all), frontal cortex, hippocampus, occipital lobe, thalamus, white matter and whole brain.

Brain kinetic analysis: Extracted brain TACs were analyzed by compartmental modeling with reversible one- (1T) and two- (2T) tissue compartment models using the measured metabolite-corrected arterial plasma input function. Each model was assessed with a vascular fraction V_f fixed to 5% and also with V_f estimated as an additional model parameter. For quantification based on compartment models, we followed the consensus nomenclature for in vivo imaging of reversibly binding radioligands[30]. The primary outcome of interest was the total volume of distribution V_T representing the equilibrium ratio of tracer concentration in tissue relative to its plasma concentration and which is linearly related to the tracer binding to the target. V_T was calculated as K_1/k_2 for a 1T compartment model and as $(K_1/k_2) \times (1 + k_3/k_4)$ for a 2T model. The Logan and multilinear 1 (MA1) graphical analysis methods utilizing arterial input function[31] were also tested as alternative techniques for estimation of V_T.

ACKNOWLEDGEMENTS

We thank David Lee and Timothy Beaudoin at the MGH Gordon PET cyclotron facility for producing fluorine-18. We thank the veterinary staff (Helen Deng) for assistance with animal handling. Funding: This study was supported by R21NS120139 (PB), K99EB033407 (YPZ), S10OD018035 (GEF, MDN), P41EB022544 (GEF, MDN) and MGH Fund for Medical Discovery (YPZ).

AUTHOR CONTRIBUTIONS

YPZ contributed to the study design, developed the automated radiosynthesis protocols, and synthesized the radiotracers; MDN: contributed to the study design, performed the PET imaging in monkeys and contributed to data interpretation; VB assisted with the PET imaging and performed initial data analysis; MTMS, YS, SHM processed and analyzed the blood samples; GEF: contributed to data interpretation; NJG processed and analyzed the PET data assisted by MTMS; PB contributed to the study design, radiosynthesis method development and data analysis and interpretation. YPZ, VB, NJG and PB wrote the manuscript and all authors reviewed and approved it.

DATA AVAILABILITY

The datasets generated and analyzed during the current study available from the corresponding authors upon reasonable request.

DISCLOSURES

YPZ and PB are named coinventor on patents concerning fluorogabapentin derivatives (PCT/US21/28455). All other authors declare no conflicts of interest related to this work.

REFERENCES

1 Dolphin, A. C. The α2δ subunits of voltage-gated calcium channels. *Biochim. Biophys. Acta* **1828**, 1541-1549, doi: https://doi.org/10.1016/j.bbamem.2012.11.019 (2013).

2 Taylor, C. P. & Garrido, R. Immunostaining of rat brain, spinal cord, sensory neurons and skeletal muscle for calcium channel alpha2-delta (α2-δ) type 1 protein. *Neuroscience* **155**, 510-521, doi: https://doi.org/10.1016/j.neuroscience.2008.05.053 (2008).

3 Alles, S. R. *et al.* Peripheral nerve injury increases contribution of L-type calcium channels to synaptic transmission in spinal lamina II: Role of α2δ–1 subunits. *Mol. Pain* **14**, 1744806918765806, doi: 10.1177/1744806918765806 (2018).

4 Yamamoto, K. *et al.* Oxaliplatin administration increases expression of the voltage-dependent calcium channel α2δ-1 subunit in the rat spinal cord. *J. Pharmacol. Sci.* **130**, 117-122, doi: https://doi.org/10.1016/j.jphs.2016.01.006 (2016).

5 D'Arco, M., Margas, W., Cassidy, J. S. & Dolphin, A. C. The Upregulation of $\alpha_2\delta$-1 Subunit Modulates Activity-Dependent Ca^{2+} Signals in Sensory Neurons. *The Journal of Neuroscience* **35**, 5891-5903, doi: 10.1523/jneurosci.3997-14.2015 (2015).

6 Boroujerdi, A. *et al.* Calcium channel alpha-2-delta-1 protein upregulation in dorsal spinal cord mediates spinal cord injury-induced neuropathic pain states. *Pain* **152**, 649-655, doi: 10.1016/j.pain.2010.12.014 (2011).

7 Boroujerdi, A. *et al.* Injury discharges regulate calcium channel alpha-2-delta-1 subunit upregulation in the dorsal horn that contributes to initiation of neuropathic pain. *Pain* **139**, 358-366, doi: https://doi.org/10.1016/j.pain.2008.05.004 (2008).

8 Newton, R. A., Bingham, S., Case, P. C., Sanger, G. J. & Lawson, S. N. Dorsal root ganglion neurons show increased expression of the calcium channel α2δ-1 subunit following partial sciatic nerve injury. *Mol. Brain Res.* **95**, 1-8, doi: https://doi.org/10.1016/S0169-328X(01)00188-7 (2001).

9 Luo, Z. D. *et al.* Upregulation of Dorsal Root Ganglion $\alpha_2\delta$ Calcium Channel Subunit and Its Correlation with Allodynia in Spinal Nerve-Injured Rats. *The Journal of Neuroscience* **21**, 1868-1875, doi: 10.1523/jneurosci.21-06-01868.2001 (2001).

10 Boudieu, L. *et al.* Blocking α2δ-1 Subunit Reduces Bladder Hypersensitivity and Inflammation in a Cystitis Mouse Model by Decreasing NF-kB Pathway Activation. *Front. Pharmacol.* **10**, doi: 10.3389/fphar.2019.00133 (2019).

11 Sekiguchi, F., Tsubota, M. & Kawabata, A. Involvement of Voltage-Gated Calcium Channels in Inflammation and Inflammatory Pain. *Biological and Pharmaceutical Bulletin* **41**, 1127-1134, doi: 10.1248/bpb.b18-00054 (2018).

12 Swartzwelder, H. S., Park, M.-H. & Acheson, S. Adolescent Ethanol Exposure Enhances NMDA Receptor-Mediated Currents in Hippocampal Neurons: Reversal by Gabapentin. *Sci. Rep.* **7**, 13133, doi: 10.1038/s41598-017-12956-6 (2017).

13 Spencer, S. *et al.* α2δ-1 Signaling in Nucleus Accumbens Is Necessary for Cocaine-Induced Relapse. *The Journal of Neuroscience* **34**, 8605-8611, doi: 10.1523/jneurosci.1204-13.2014 (2014).

14 Katsura, M., Shibasaki, M., Kurokawa, K., Tsujimura, A. & Ohkuma, S. Up-regulation of L-type high voltage-gated calcium channel subunits by sustained exposure to 1,4- and 1,5-benzodiazepines in cerebrocortical neurons. *J. Neurochem.* **103**, 2518-2528, doi: https://doi.org/10.1111/j.1471-4159.2007.04984.x (2007).

15 Shibasaki, M., Katsura, M., Tsujimura, A. & Ohkuma, S. Up-regulated l-type high voltage-gated calcium channels cause increase in diazepam binding inhibitor induced by sustained morphine exposure in mouse cerebrocortical neurons. *Life Sci.* **80**, 166-172, doi: https://doi.org/10.1016/j.lfs.2006.08.036 (2006).

16 Katsura, M. *et al.* Ethanol physical dependence is accompanied by up-regulated expression of L-type high voltage-gated calcium channel α1 subunits in mouse brain. *Brain Res.* **1039**, 211-215, doi: https://doi.org/10.1016/j.brainres.2005.01.074 (2005).

17 Hayashida, S., Katsura, M., Torigoe, F., Tsujimura, A. & Ohkuma, S. Increased expression of L-type high voltage-gated calcium channel α1 and α2/δ subunits in mouse brain after chronic nicotine administration. *Mol. Brain Res.* **135**, 280-284, doi: https://doi.org/10.1016/j.molbrainres.2004.11.002 (2005).

18 Nieto-Rostro, M. *et al.* Altered expression of the voltage-gated calcium channel subunit α2δ-1: A comparison between two experimental models of epilepsy and a sensory nerve ligation model of

neuropathic pain. *Neuroscience* **283**, 124-137, doi: https://doi.org/10.1016/j.neuroscience.2014.03.013 (2014).

19 Dickens, D. *et al.* Transport of gabapentin by LAT1 (SLC7A5). *Biochem Pharmacol* **85**, 1672-1683, doi:10.1016/j.bcp.2013.03.022 (2013).

20 Zhou, Y.-P. *et al.* Development of a PET radioligand for α2δ-1 subunit of calcium channels for imaging neuropathic pain. *Eur. J. Med. Chem.* **242**, 114688, doi: https://doi.org/10.1016/j.ejmech.2022.114688 (2022).

21 Collier, T., Normandin, M., El Fakhri, G. & Vasdev, N. Automation of column-switching HPLC for analysis of radiopharmaceuticals and their metabolites in plasma. *J. Nucl. Med.* **54**, 1133-1133 (2013).

22 Hilton, J. *et al.* Column-switching HPLC for the analysis of plasma in PET imaging studies. *Nucl. Med. Biol.* **27**, 627-630, doi: https://doi.org/10.1016/S0969-8051(00)00125-6 (2000).

23 Guehl, N. J. *et al.* Radiochemical Synthesis and Evaluation in Non-Human Primates of 3-[^{11}C]methoxy-4-aminopyridine: A Novel PET Tracer for Imaging Potassium Channels in the CNS. *ACS Chem. Neurosci.* **12**, 756-765, doi: 10.1021/acschemneuro.0c00791 (2021).

24 Guehl, N. J. *et al.* Evaluation of the potassium channel tracer [^{18}F]3F4AP in rhesus macaques. *J. Cereb. Blood Flow Metab.* **41**, 1721-1733, doi: 10.1177/0271678x20963404 (2021).

25 Jenkinson, M., Beckmann, C. F., Behrens, T. E. J., Woolrich, M. W. & Smith, S. M. FSL. *NeuroImage* **62**, 782-790, doi: https://doi.org/10.1016/j.neuroimage.2011.09.015 (2012).

26 Seidlitz, J. *et al.* A population MRI brain template and analysis tools for the macaque. *NeuroImage* **170**, 121-131, doi: https://doi.org/10.1016/j.neuroimage.2017.04.063 (2018).

27 Paxinos, G., Huang, X. & Toga, A. W. (1999). The Rhesus Monkey Brain in Stereotaxic Coordinates. San Diego, USA: Academic Press.

28 McLaren, D. G. *et al.* A population-average MRI-based atlas collection of the rhesus macaque. *NeuroImage* **45**, 52-59, doi: https://doi.org/10.1016/j.neuroimage.2008.10.058 (2009).

29 Rohlfing, T. *et al.* The INIA19 Template and NeuroMaps Atlas for Primate Brain Image Parcellation and Spatial Normalization. *Front. Neuroinform.* **6**, doi: 10.3389/fninf.2012.00027 (2012).

30 Innis, R. B. *et al.* Consensus Nomenclature for in vivo Imaging of Reversibly Binding Radioligands. *J. Cereb. Blood Flow Metab.* **27**, 1533-1539, doi: 10.1038/sj.jcbfm.9600493 (2007).

31 Logan, J. *et al.* Graphical Analysis of Reversible Radioligand Binding from Time—Activity Measurements Applied to [N-^{11}C-Methyl]-(−)-Cocaine PET Studies in Human Subjects. *J. Cereb. Blood Flow Metab.* **10**, 740-747, doi: 10.1038/jcbfm.1990.127 (1990).